Nanoscale

Accepted Manuscript

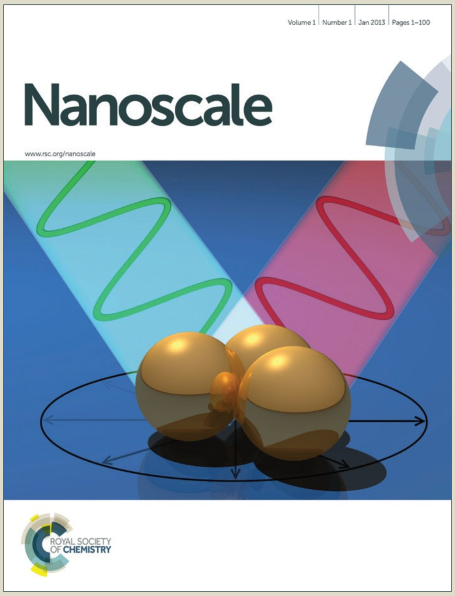

ROYAL SOCIETY OF CHEMISTRY

www.rsc.org/nanoscale

Nanoscale RSCPublishing

ARTICLE

Pt Skin on Pd-Co-Zn/C Ternary Nanoparticles with Enhanced Pt Efficiency for the Oxygen Reduction Reaction

Cite this: DOI: 10.1039/x0xx00000x

Received 00th January 2012,
Accepted 00th January 2012

DOI: 10.1039/x0xx00000x

www.rsc.org/

Weiping Xiao,[a] Jing Zhu,[a] Lili Han,[b] Sufen Liu,[a] Jie Wang,[a] Zexing Wu,[a] Wen Lei,[a] Cuijuan Xuan,[a] Huolin Xin,[b] and Deli Wang [a,]*

Exploring highly active, stable and relative low-cost nanomaterials for the oxygen reduction reaction (ORR) is of vital importance for the commercialization of proton exchange membrane fuel cells (PEMFCs). Herein, a highly active, durable, carbon supported, and monolayer Pt coated Pd-Co-Zn nanoparticle is synthesized via a simple impregnation-reduction method, followed by a spontaneous displacement of Pt. By tuning the atomic ratios, we obtain the composition-activity volcano curve for the Pd-Co-Zn nanoparticles and determined that Pd:Co:Zn=8:1:1 is the optimal composition. Compared with pure Pd/C, the Pd_8CoZn/C nanoparticles show a substantial enhancement in both the catalytic activity and the durability toward the ORR. Moreover, the durability and activity are further enhanced by forming a Pt skin on Pd_8CoZn/C nanocatalysts. Interestingly, after 10,000 potential cycles in N_2-saturated 0.1 M $HClO_4$ solution, $Pd_8CoZn@Pt/C$ shows improved mass activity (2.62 A mg^{-1}_{Pt}) and specific activity (4.76 A m^{-2}_{total}), which are about 1.4 and 4.4 times higher than the initial values, and 37.4 and 5.5 times higher than those of Pt/C catalysts, respectively. After accelerated stability testing in O_2-saturated 0.1 M $HClO_4$ solution for 30,000 potential cycles, the half-wave potential negatively shifts about 6 mV. The results show that the Pt skin plays an important role in enhancing the activity as well as preventing degradation.

1 Introduction

Proton exchange membrane fuel cells (PEMFCs) have been considered as the next-generation power supply devices due to their high-energy density, high-energy conversion efficiency, environmentally friendly and relative low working temperature[1-3]. However, it remains a challenge to commercialize this advanced technology on a large scale owing to the high cost and the rarity of Pt catalyst. Pt is one of the key elements on both anode and cathode electrocatalysts, especially in the cathode material to accelerate the sluggish kinetics of the oxygen reduction reaction (ORR)[4-6]. Currently, the promising strategy to develop high-performance and less-expensive ORR catalysts is to design Pt surface-enriched nanoparticles with so-called skin, non-precious metal electrocatalysts, or noble metal alloy nanocatalyst[7,8]. Among these catalysts, the most promising tactics is to design core-shell structure catalyst with non-Pt core and ultrathin Pt shell. Accordingly, monolayer Pt shell supported on less expensive metal core can combine the advantages of Pt and non-Pt metals and exhibit excellent activity through the interaction between the shell and the core, such as ligand effect and strain effect[9-13].

Recently, much effect has been devoted to the relative low-cost Pd-based nanocatalysts based on the similar lattice constant and chemical property of Pd with Pt [14,15]. Both theoretical and experimental studies have shown that incorporation of Pd and Pt can lower the surface electronic d-band center of Pt to bring in the enhancement of catalytic activity for ORR[16,17]. Hence, replacing the bulk Pt with less expensive metal (such as Pd) could not only improve the utilization of Pt but also obtain excellent catalyst activity[18]. Xia and coworkers[19] have successfully prepared Pt shell with 2-3 atomic layers on Pd nanocube core with improved ORR activity and the ORR specific activity. Similar structures have also been achieved by Yu and co-workers, who design ultrathin and uniform Pd@Pt nanowires with controllable composition and shell thickness[20]. Another elegant approach was applied to design $Pd@Pt_{1.8}Ni$ core-shell nanocrystals with Pt alloy shell and octahedral Pd[11]. In addition to improve the catalytic activity, the existence of Pd could prevent Pt from corrosion by sacrificing Pd or up-shifting the dissolution potential of Pt, and thus, enhancing the catalytic durability[21]. In certain cases, the activity of synthesized materials is largely attributed to the synergistic effect and ultrathin Pt shell. Although a range of techniques have been developed to produce core-shell nanostructures, the core-shell structure with high active core is rarely reported. Moreover, the catalyst with ultra-uniform particle size distribution by using a facile and large scale synthetic strategy remains a challenge. Based on this, it is of vital importance to design core-shell particles with high active Pd-based core and ultrathin Pt shell using a facile method. Similar to Pt, by incorporating a secondary metal element (such as Ni, Cu, Co, et al.) to form Pd-based alloy, the d-band center and surface atomic arrangement of Pd will play an important role in the ORR kinetics, and then improve the catalytic activity[22].

Herein, a facile impregnation reduction and spontaneous replacement method is demonstrated to synthesize $Pd_8CoZn@Pt/C$ core-shell nanocatalyst with monolayer Pt shell. By tuning the atomic ratio of Pd to Co and Zn, the controllable composition of Pd-based ternary alloys with different alloying degree are obtained. The higher alloying degree of Pd-based catalyst could decrease the binding strength of OH_{ads} and then increase ORR activity. Thus, a volcano-type relationship between the ORR catalyst activity and the ratio of different atoms is obtained and revealed well with ligand effect. The Pd_8CoZn/C nanoparticles show the best performance among Pd-Co-Zn/C series catalysts in both catalytic activity and durability toward the ORR. By simply adjusting reaction temperature and the amounts of Pt precursors added into Pd_8CoZn/C nanoparticles, the Pt-shell structure is successfully achieved by spontaneous replacement reaction. The designed $Pd_8CoZn@Pt$ core-shell structure nanoparticles exhibit ultra-high electrocatalytic activity and stability for ORR, which is attributed to the high active core and the single atomic layer Pt shell.

2 Experimental Section

2.1 Material Synthesis

Pd/C and Pd-based ternary nanoparticles were synthesized by using a simple impregnation reduction method. In a typical synthesis for Pd_8CoZn/C nanoparticles, $PdCl_2$ (Aldrich), $ZnCl_2$ (Aldrich) and $CoCl_2{\cdot}6H_2O$ (Aldrich) with a molar ratio of 8:1:1 were dissolved in 10 mL of ultra-pure water and then Vulcan XC-72 carbon support was added into the solution to obtain 20 wt.% Pd. After interchanging magnetic stirring at 60 °C with ultrasonic blending, a smooth thick slurry was obtained and then dried in vacuum oven overnight. The powder was grinded in a agate mortal and then reduced in a tube furnace under flowing H_2/Ar atmosphere at 300 °C for 2 h, followed by a heat treatment at 500 °C for 10 h. Pd_8CoZn/C nanoparticles were collected after cooling down to room temperature under N_2 atmosphere. For comparison, Pd/C, Pd_4CoZn/C and $Pd_{12}CoZn/C$ were synthesized using the same procedure. $Pd_8CoZn@Pt/C$ catalyst was obtained by using a spontaneous displacement reaction. In detail, 50 mg of as-prepared Pd_8CoZn/C sample was dispersed in a certain amount of K_2PtCl_4 solution by controlling the Pt to Pd nominal atomic ratio of 1:80. After ultrasonic blending for 30 min, the suspension was heated at 70 °C under magnetic stirring for 3 h with N_2 protection. Then, the suspension was centrifuged with ultra-pure water and dried in a vacuum oven at 60 °C for 10 h.

2.2 Physical Characterization

Powder X-Ray diffraction (XRD) patterns of the as-prepared catalysts were obtained on an X'Pert PRO diffractometer using a Cu Kα radiation source. The diffraction patterns were collected from 15^o to 85^o at a scanning rate of 4^o min^{-1}. Transmission electron microscopy (TEM) measurements were performed on a Tecnai G320 TEM operated at 300 kV by drop casting the nanoparticle dispersions on carbon-coated Cu grids and drying under ambient conditions. Thermal gravimetric analysis (TGA) was conducted on a TA Q500 Instrument at a heating rate of 10 °C min^{-1}. ICP-AES was investigated by using IRIS Advantage (Thermo Elemental Co. USA).

2.3 Electrochemical Measurements

The catalyst was suspended in a mixture of isopropanol/Nafion (0.1 % Nafion) hybrid solutions to form a homogeneous ink. 7.8 μL of the suspension (5 mg mL^{-1}) was deposited on a pre-cleaned glassy carbon RDE with a diameter of 5 mm and dried naturally. A Pt wire was used as the counter electrode and a reversible hydrogen electrode (RHE) was used as the reference electrode. Electrochemical measurements were conducted in 0.1 M $HClO_4$ solution at 25 ± 0.5 °C. The catalyst was first cycled at 50 mV s^{-1} between 0.05 V and 1.1 V until stable cyclic voltammograms (CVs) were obtained. Then, CVs and CO-stripping voltammetry were measured in N_2-saturated 0.1 M $HClO_4$ solution at a scan rate of 50 mV s^{-1}. Linear scan voltammetry was conducted in O_2-saturated 0.1 M $HClO_4$ solution in the potential ranging from +0.2 V to +1.0 V at a scan rate of 5 mV s^{-1} and rotation rate of 1600 rpm. The durability test was conducted by cycling the potentials between 0.05 and 1.1 V at a rate of 50 mV s^{-1} in N_2-saturated 0.1 M $HClO_4$ for 10 K cycles. Mass or specific activities were obtained at 0.85 and 0.90 V and depicted as kinetic current densities normalized to Pd or Pt mass loading or to the electrochemical active surface area (ECSA) obtained from hydrogen region measurement.

3 Results and Discussion

The Pd_xCoZn/C series nanocatalysts with controllable metal ratio ranging from 4:1:1 to 12:1:1 was synthesized as illustrated in Fig. S1[23]. When annealed at 500 °C under H_2/Ar atmosphere, the as-prepared Pd_xCoZn/C catalysts spontaneously formed Pd-rich shell, which could be attributed by the larger adsorption enthalpy of H on Pd than on Co and Zn as the theoretical expectations[24,25]. Moreover, the electron energy-loss spectroscopic (EELS) elemental mapping had been employed to confirm the presence of a Pd-rich shell on the Pd-based nanoparticles.

The bulk physical analysis of the Pd_xCoZn/C series nanocatalysts were conducted using X-ray diffraction (XRD), which had stripped the Cu Kα2 pattern. All of the samples, except Pd_4CoZn/C, showed a typical face-centered-cubic (fcc) pattern. As can be seen from Fig. 1a, the broad peak at around 25^o was attributed to the carbon support and the other diffraction peaks located at 40.08^o, 46.64^o, 68.12^o and 82.09^o corresponded to the (111), (200), (220) and (311) planes of Pd with fcc phase, respectively. In addition to Pd alloy phase in Pd_4CoZn/C catalyst, PdZn intermetallic phase and pure Co phase were also observed possibly due to the high content of Zn and Co. The peaks position of Pd_8CoZn/C and $Pd_{12}CoZn/C$ nanoparticles shifted to higher angles relative to Pd/C, which could be clearly seen in the expanded (220) diffraction peaks displayed in Fig. 1b, indicating alloy phases were formed between Pd and the smaller atoms (Co, Zn), resulting in a contracted Pd lattice. Consequently, a volcano-type relationship between the lattice parameters of Pd and the ratio of different atoms was obtained and the alloy degree of Pd_8CoZn/C was larger than that of $Pd_{12}CoZn/C$ and Pd_4CoZn/C (Table S1 and insert of Fig 2b). Furthermore, by using Debye-Scherrerequation[26], the domain size of Pd, Pd_8CoZn/C and $Pd_{12}CoZn/C$ nanoparticles from the XRD data was calculated to be 15.0, 10.3 and 11.2 nm, respectively, as shown in Table S1.

The structures of the carbon-supported Pd_8CoZn/C nanoparticles were examined using a scanning transmission electron microscope (STEM) equipped with an Enfina electron energy loss spectrometer (EELS). As shown in the overview TEM image in Fig. 1c, the nanoparticles presented a uniform spherical-like morphology and were well dispersed on the surface of the carbon support. In addition, Fig. 1d presented the particle size distribution of Pd_8CoZn/C nanoparticles between 3 nm and 16 nm with an average particle size of 9.2 nm, which was calculated from more than 200 nanoparticles. EELS elemental maps (Fig. 1e, f, g and h) of one Pd_8CoZn/C particle, performed on a fifth-order aberration corrected STEM instrument operated at 100 kV, clearly showed that a Pd-rich shell with evenly distributed Co and Zn inside the particle. For Pd-based multi-metallic nanocrystals, the electro-catalysis properties, including ORR activities, are known to be highly dependent on the elemental composition. Therefore, the atomic ratio of Pd, Co and Zn was tuned in order to optimize the obtained Pd_xCoZn/C series catalysts. The electrocatalytic ORR performance of the as-obtained catalysts was measured and compared with the Pt/C (20 wt. %). The CVs of Pd/C and Pd_xCoZn/C series catalysts were shown in Fig. 2a. It can be seen that the hydrogen adsorption of Pd was inhibited by the incorporated Co and Zn. Furthermore, when compared to Pd/C, in the cathodic scan, the peak potential, for the reduction of Pd surface oxides first shifted positive and then slightly negative with the decrease of Co and Zn content. The peak potential for the reduction of surface oxides is related to the binding strength of oxygen on the metal surface. It has been reported that a shift of the reduction peak of the surface oxides to higher potentials reflects a decrease in the adsorption strength for the oxygen-containing species on the surface [27-29]. Pd_8CoZn/C exhibited the most positive shift of the potential among all the catalysts. A volcano-type relationship between the peak potential of Pd oxides reduction and the ratio of different atoms was obtained (insert in Fig. 2b). Fig. 2b showed linear sweep voltammograms (LSV) for different Pd_xCoZn/C catalysts compared with commercial Pt/C. All of the Pd_xCoZn/C catalysts exhibited lower ORR overpotentials than that on Pd/C catalyst and the half-wave potentials of Pd_4CoZn/C, Pd_8CoZn/C and $Pd_{12}CoZn/C$ showed a significant positive shift of 32 mV, 56 mV and 43 mV, respectively, and a slightly lower half-wave potentials than Pt/C, indicating that the alloying of Pd with Co and Zn led to an increased ORR activity (Table S2).

In order to better understand the relationship between lattice-strain and catalyst activity, we calculated the kinetic currents from the ORR polarization curves by following the Koutecky-Levich equation[30] and then normalized the kinetic current to the mass and the ECSA of Pd, corresponding to mass activity (MA, Fig. 2c) and specific activity (SA, Fig. 2d), respectively. Accordingly, the MA and SA of Pd_xCoZn/C catalysts displayed a marked exaltation relative to Pd/C, demonstrating that Pd_xCoZn/C nanoparticles could substantially enhance Pd utilization. Importantly, the values of MA and SA on Pd_8CoZn/C at 0.85 V were 5.8 and 8.2 times higher than that on Pd/C, indicating that Pd alloy surface exhibited more desirable surface which was favorable for the ORR (Table S2). The reduced lattice constant or the raised alloying degree may decrease the binding strength of OH_{ads}, and thus increase the ORR activity. The unsatisfactory catalytic activity of Pd_4CoZn/C and $Pd_{12}CoZn/C$ was probably due to the lower alloying degree (Fig. 1b and table S1) or larger particle size (Table S1). A volcano-type relationship between the ORR catalyst activity and the ratio of different atoms as shown in the insert of Fig. 2c and the Pd_8CoZn/C nanoparticles exhibited the highest electro-catalytic activity toward ORR.

The durability of Pd/C and Pd_8CoZn/C catalyst was evaluated by applying a potential cycling between 0.05 and 1.1 V at a scan rate of rate of 50 mV s^{-1} in N_2-saturated 0.1 M $HClO_4$ solution. Fig. S2a and Fig. 3a showed the CV curves change of Pd/C and Pd_8CoZn/C during cycling. The current in the hydrogen region diminished quickly with cycling. And the ECSA of Pd/C and Pd_8CoZn/C reduced about 79% and 34% of the initial surface area after 1000 potential cycles, as can be seen in the inserts of Fig. S2a and Fig. 3a. The ORR polarization curves on Pd/C and Pd_8CoZn/C electrodes before and after 1 K cycles were shown in Fig. S2b and Fig. 3c, respectively. The half-wave potential on Pd/C electrode showed a 58 mV negative shift after cycling, while on Pd_8CoZn/C electrode, the potential decayed about 29 mV. The durability test was also conducted in O_2-saturated 0.1 M $HClO_4$ solution between 0.6 V and 1.0 V at a scan rate of 50 mV s^{-1} for 1,000 potential cycles. It can be seen from the CVs change in Fig. 3b that the ECSA of Pd_8CoZn/C reduced 41% of the initial surface area after 1000 potential cycles, as can be seen in the inserts of Fig. 3b. The ORR durability in Fig. 3d shows a significant negative shift of the half-wave potential about 35 mV after 1000 potential cycling, indicating that the decay of the catalytic activity was accelerated on Pd_8CoZn/C in oxidized condition. Above analysis clearly showed that by incorporation of Co and Zn in Pd lattice, the obtained Pd_8CoZn/C catalyst exhibited enhanced electro-catalytic activity and desirable stability toward ORR compared to Pd/C.

In order to further improve the ORR activity and durability of Pd_8CoZn/C catalyst, a trace amount of Pt was decorated on the surface of Pd_8CoZn/C (denoted as $Pd_8CoZn@Pt/C$) by using a spontaneous replacement method. The presence of monolayer of Pt was verified by ICP-AES and EELS elemental mapping (Fig. S5 and Fig. 4g), although the amount of Pt was too small to be detected using XRD (Fig. S3). Fig. 4a showed the overview TEM image of $Pd_8CoZn@Pt/C$ nanoparticles. It can be seen that the nanoparticles dispersed well on the surface of carbon support and the Pd-based cores retained their original spherical shape after Pt decoration. The corresponding HRTEM micrograph of an individual particle for $Pd_8CoZn@Pt/C$ was shown in Fig. 4b and the lattice spacing of 2.23 Å could be indexed to Pd (111) plane, which was in agree with the XRD patterns. The atomic-scale chemical maps of Pd, Co, Zn and the composite in Fig. 4d, e, f and g clearly showed a Pt-rich shell with evenly distributed Pd, Co and Zn inside the particle, consistent with the idealized atomic structure of the $Pd_8CoZn@Pt/C$ core-shell nanoparticle (Fig. 4c). Furthermore, we can see from Fig. S4 that the Pd, Co, and Zn signals emerged simultaneously, and the strongest signals appeared at the central position of the particle. However, Pt exhibited a different scanning spectrum, with two symmetric peaks, confirming the core-shell structure of the $Pd_8CoZn@Pt$ particle. The atomic ratio of Pd and Pt was measured to be 35:1 from the elemental analysis (Fig. S5 and Table S3). Moreover, a quantitative analysis of the atomic ratio of Pd and Pt was measured to be 86.2:1 from the inductively coupled plasma mass spectrometry (ICP-AES) (Table S3), which was close to the nominal ratio of 80:1, corresponding to a monolayer of Pt shell on the surface of Pd_8CoZn/C nanoparticles.

Fig. 5a showed the CV curves comparison of Pd_8CoZn/C before and after monolayer Pt decoration. It can be seen that $Pd_8CoZn@Pt/C$ electrode exhibited a positive shift of surface oxides reduction potential relative to Pd_8CoZn/C, indicating the weaker adsorption strength for the oxygen-containing species on the metal surface after Pt decoration. Moreover, the peak potential for CO stripping on $Pd_8CoZn@Pt/C$ electrode showed a negative shift than that on Pd_8CoZn/C, further suggesting a successful Pt decoration and weakening the CO adsorption energy as shown in Fig. 5b. Fig. 5c compared the ORR polarization curves on Pd/C, Pt/C, Pd_8CoZn/C and

$Pd_8CoZn@Pt/C$ electrodes. The half-wave potential of $Pd_8CoZn@Pt/C$ exhibited a significant positive shift of 20 mV after Pt decoration, which was comparable to Pt/C. Since the adsorbed OH species could reduce the ORR activity, the lower OH_{ads} coverage on the surface of the $Pd_8CoZn@Pt/C$ catalysts would exhibit faster ORR kinetics. Therefore, a combination between Pd and Pt can lower the d-band center of Pt and then enhance the ORR activity[1, 31].

As shown in Fig. 5d and Fig. 5e, the MA and SA of $Pd_8CoZn@Pt/C$ nanoparticles, calculated from the Koutecky-Levich, displayed a marked exaltation relative to Pt/C. Interestingly, the values of MA and SA the $Pd_8CoZn@Pt/C$ were 26.7 and 1.3 times of the Pt/C at 0.9 V (inset in Fig. 5d,e and Table 1), respectively. Furthermore, the rotation-rate-dependent current-potential curves of the $Pd_8CoZn@Pt/C$ nanoparticles were shown in the insert of Fig. 5f and the number of electrons transferred (n) is calculated to be nearly 4.0 at potential range from 0.75 to 0.825 V, indicating the nearly complete reduction of O_2 to H_2O on the surface of $Pd_8CoZn@Pt/C$.

Table 1 electrochemical results of Pt/C and $Pd_8CoZn@Pt/C$

Catalyst	ECSA ($m^2\ g^{-1}_{total}$)	SA ($A\ m^{-2}_{total}$)		MA ($A\ mg^{-1}_{Pt}$)	
		0.85 V	0.9 V	0.85 V	0.9 V
Pt/C	79.7	4.2	0.87	0.34	0.07
$Pd_8CoZn@Pt/C$	40.1	5.9	1.08	10.35	1.89
$Pd_8CoZn@Pt/C$-1 K	34.0	7.7	1.46	11.36	2.18
$Pd_8CoZn@Pt/C$-5 K	14.0	23.1	4.26	14.10	2.59
$Pd_8CoZn@Pt/C$-10 K	12.6	24.0	4.76	13.18	2.62

The stabilizing effect of Pt on the Pd_6CoCu/C nanoparticles was evaluated by cycling the electrode in both N_2- and O_2-saturated 0.1 M $HClO_4$ solution, respectively. As shown in Fig. 6a, the half-wave potential in N_2 atmosphere shifted positively about 5 mV after 1 K cycles, further shifted about 11 mV after 5 K cycles relative to initial value and stabilizes at 0.874 V. The enhanced catalytic activity for ORR could be attributed to the exposure of more active sites of decorated Pt during cycling, which was confirmed by CO stripping voltammetry as shown in Fig. 6b. Furthermore, the peak potential for CO stripping on $Pd_8CoZn@Pt/C$ electrode shifted negatively with cycling and the peak potential was 0.83 V after 10 K cycles, comparable to that of pure Pt (Fig. S6), suggesting that the surface was more Pt-rich with cycling, which played an important role in stabilizing the catalyst. In contrast, the half-wave potential of commercial Pt/C suffered a loss of 22 mV after 10 K cycles compared with the initial value (Fig. S7). The ECSAs of the $Pd_8CoZn@Pt/C$ decreased with cycling, indicating the dissolution of Pd, Co and Zn (Table 1). However, the MA based on Pt loading ($I_{k,}$ Fig. 6c) and SA ($I_{k,}$ Fig. 6d) of $Pd_8CoZn@Pt/C$ enhanced with cycling compared with the initial value. Interestingly, after 10 K potential cycles, the MA (2.62 $A\ mg^{-1}_{Pt}$) and SA (4.76 $A\ m^{-2}_{total}$) of $Pd_8CoZn@Pt/C$ increased about of 1.4 and 4.4 times than the initial values, and 37.4 and 5.5 times higher than those on Pt/C catalysts. The enhancement of activity could be attributed to the strain arising from the mismatch in lattice constant between the Pd_8CoZn/C core and ultrathin Pt shell. After testing the electrode for 30 K potential cycles in O_2-saturated 0.1 M $HClO_4$ solution between 0.6 V and 1.0 V at a scan rate of 50 mV s^{-1} (Fig. 6e), the half-wave potential negatively shifts about 6 mV, which is much lower than that of the Pd_8CoZn/C electrode cycled only 1 K cycles (35 mV), indicating the enhanced stability of Pd_8CoZn/C after Pt decoration on the surface. The MA of $Pd_8CoZn@Pt/C$ at 0.9 V ($i_{k,}$ Fig. 6f) decreased from 1.89 $A\ mg^{-1}_{Pt}$ to 1.56 $A\ mg^{-1}_{Pt}$ after 30 K cycles, which is slightly higher than that in N_2-saturated 0.1 M $HClO_4$ solution, indicating that the decay of the catalytic activity was accelerated in oxidized condition.

The morphology of $Pd_8CoZn@Pt/C$ catalyst exhibited almost no obvious change after 10 K potential cycles (Fig. 7a). Fig. 7b showed the HRTEM image of an individual $Pd_8CoZn@Pt/C$ nanoparticle. The interplanar spacings are measured to be 2.23 Å and 2.28 Å from HRTEM image, corresponding to Pd (1,1,1) plane and Pt (1,1,1) plane, respectively. Consistent with the result from CO stripping voltammetry (Fig. 6b), the surface was Pt-rich during potential cycling. Furthermore, the atomic-scale chemical maps (Fig. 7d, e, f, g and h) of one $Pd_8CoZn@Pt/C$ particle (Fig. 7c) clearly show a Pt-rich shell. Therefore, it can be concluded that the Pt-rich shell was still integral, inhibiting the corrosion of the Pd_8CoZn/C core, and resulting in the enhancement of catalytic activity and stability.

Conclusions

In summary, Pd-based ternary electrocatalysts have been successfully synthesized with different Pd alloying degree. Pd_8CoZn/C nanoparticle exhibits the best ORR activity among the Pd-based electrocatalysts and enhanced stability than that of Pd/C. The activity and stability of Pd_8CoZn/C nanoparticle was further improved by atomic layer of Pt decoration. As a result, the Pt mass activity on $Pd_8CoZn@Pt/C$ is about 27 times higher than that on Pt/C. Moreover, the $Pd_8CoZn@Pt/C$ catalysts exhibited excellent stability for the ORR under potential cycling both in N_2- and O_2-saturated 0.1 M $HClO_4$ solution. This extraordinary ORR electrocatalytic activity and durability can be attributed to a compressive strain effect originating from the interaction between the monolayer Pt shell and the Pd_8CoZn core. We believe that the facile synthetic strategy could be extended to other multi-metallic nanocrystals, making it possible to design highly active catalysts beyond fuel cell applications.

Acknowledgements

This work was supported by the National Natural Science Foundation (21306060, 21573083), the Program for New Century Excellent Talents in Universities of China (NCET-13-0237), the Doctoral Fund of Ministry of Education of China (20130142120039), the Fundamental Research Funds for the Central University (2013TS136, 2014YQ009). We thank Analytical and Testing Center of Huazhong University of Science and Technology for allowing us to use its facilities. S/TEM work was carried out at the Center for Functional Nanomaterials, Brookhaven National Laboratory, which is supported by the U.S. Department of Energy, Office of Basic Energy Sciences, under Contract No.DE-SC0012704.

Notes and references

[a] Key laboratory of Material Chemistry for Energy Conversion and Storage (Huazhong University of Science and Technology), Ministry of Education, Hubei Key Laboratory of Material Chemistry and Service Failure, School of Chemistry and Chemical Engineering, Huazhong University of Science and Technology, Wuhan, 430074, P.R. China.
E-mail: wangdl81125@hust.edu.cn.
[b] Center for Functional Nanomaterials, Brookhaven National Laboratory, Upton, NY 11973, USA

Electronic Supplementary Information (ESI) available: [details of illustration of the synthesis procedure, electrochemical performance and TGA curve]. See DOI: 10.1039/c000000x/

1 Y. Nie, L. Li, Z. Wei, *Chem. Soc. Rev.* 2015, **44**, 2168-2201.

2 H.l. Liu, F. Nosheen, X. Wang, *Chem. Soc. Rev.* 2015, **44**, 3056-3078.

3 B.C. Steele, A. Heinzel, *Nature* 2001, **414**, 345-352.

4 Y.J. Wang, N. Zhao, B. Fang, H. Li, X.T. Bi, H. Wang, *Chem. Rev.* 2015, **115**, 3433-3467.

5 S. Guo, S. Zhang, S. Sun, *Angew. Chem.* 2013, **52**, 8526-8544.

6 X. Zhao, S. Chen, Z. Fang, J. Ding, W. Sang, Y. Wang, J. Zhao, Z. Peng, J. Zeng, *J. Am. Chem. Soc.* 2015, **137,** 2804-2807.

7 S. Xie, S.I. Choi, N. Lu, L.T. Roling, J.A. Herron, L. Zhang, J. Park, J. Wang, M.J. Kim, Z. Xie, M. Mavrikakis, Y. Xia, *Nano. Lett.* 2014, **14**, 3570-3576.

8 X. Huang, Z. Zhao, L. Cao, Y. Chen, E. Zhu, Z. Lin, M. Li, A. Yan, A. Zettl, Y.M. Wang, X. Duan, T. Mueller, Y. Huang, *Science* 2015, **348**, 1230-1234.

9 Z. Chen, D. Higgins, A. Yu, L. Zhang, J. Zhang, *Energy Environ. Sci.* 2011, **4**, 3167-3192.

10 Y. Liang, Y. Li, H. Wang, J. Zhou, J. Wang, T. Regier, H. Dai, *Nat. Mater.* 2011, **10**, 780-786.

11 J. Son, S. Cho, C. Lee, Y. Lee, J.H. Shim, *Langmuir* 2014, **30**, 3579-3588.

12 J. Park, L. Zhang, S.I. Choi, L.T. Roling, N. Lu, J.A. Herron, S. Xie, J. Wang, M.J. Kim, M. Mavrikakis, *ACS. Nano* 2015, **9**, 2635-2647.

13 Y.J. Si, C.G. Chen, W. Yin, H. Cai, *Chinese Chem. Lett.* 2010, **21**, 983-986.

14 H. Zhang, M. Jin, Y. Xia, *Chem. Soc. Rev.* 2012, **41**, 8035-8049.

15 K J Datta, K K R Datta, M B Gawande, *Chem.-Eur. J.* 2016, **22**, 1864-1864.

16 B. Lim, M. Jiang, P.H. Camargo, E.C. Cho, J. Tao, X. Lu, Y. Zhu, Y. Xia, *Science* 2009, **324**, 1302-1305.

17 X. Wang, Y. Orikasa, Y. Takesue, H. Inoue, M. Nakamura, T. Minato, N. Hoshi, Y. Uchimoto, *J. Am. Chem. Soc.* 2013, **135**, 5938-5941.

18 K. Sasaki, H. Naohara, Y. Choi, Y. Cai, W.-F. Chen, P. Liu, R.R. Adzic, *Nat. Commun.* 2012, **3**, 1115.

19 S. Xie, S.I. Choi, N. Lu, L.T. Roling, J.A. Herron, L. Zhang, J. Park, J. Wang, M.J. Kim, Z. Xie, *Nano Lett.* 2014, **14**, 3570-3576.

20 H.H. Li, S.Y. Ma, Q.Q. Fu, X.J. Liu, L. Wu, S.-H. Yu, *J. Am. Chem. Soc.* 2015, **137**, 7862-7868.

21 X. Wang, M.I. Vara, M. Luo, H. Huang, A. Ruditskiy, J. Park, S.-X. Bao, J. Liu, J.Y. Howe, M. Chi, *J. Am. Chem. Soc.* 2015*,* **137**, 15036-15042.

22 G. Jiang, H. Zhu, X. Zhang, B. Shen, L. Wu, S. Zhang, G. Lu, Z. Wu, S. Sun, *ACS Nano* 2015, **9***,* 11014-11022.

23. D.Wang, L. Zhuang, *J. Phys. Chem. C.* 2007**, 111**, 16416-16422.

24 M. Johansson, O. Lytken, I. Chorkendorff, *J. Chem. Phys.* 2008, **128**, 034706.

25 L.L. Wang, D.D. Johnson, *J. Am. Chem. Soc.* 2009, **131**, 14023-14029.

26 S.Y. Shen, T.S. Zhao, J.B Xu, *J. Power Sources* 2010, **195***,* 1001-1006.

27 A. Aricò, A. Stassi, E. Modica, R. Ornelas, I. Gatto, E. Passalacqua, V. Antonucci, *J. Power Sources* 2008, **178**, 525-536.

28 V. Stamenkovic; T. J. Schmidt; P. N. Ross; N. M Markovic. J. Phys. Chem. B, 2002, **106**, 11970.

29 H. A. Gasteiger; S. S. Kocha; B. Sompalli; F. T Wagner. Appl.Catal., B, 2005, **56**, 9.

30 H.A. Gasteiger, S.S. Kocha, B. Sompalli, F.T. Wagner, Appl. Catal. B: Environ. 2005, **56**, 9-35.

31 J.X. Wang, H. Inada, L. Wu, Y. Zhu, Y. Choi, P. Liu, W.-P. Zhou, R.R. Adzic, J. Am. Chem. Soc. 2009, **131**, 17298-17302.

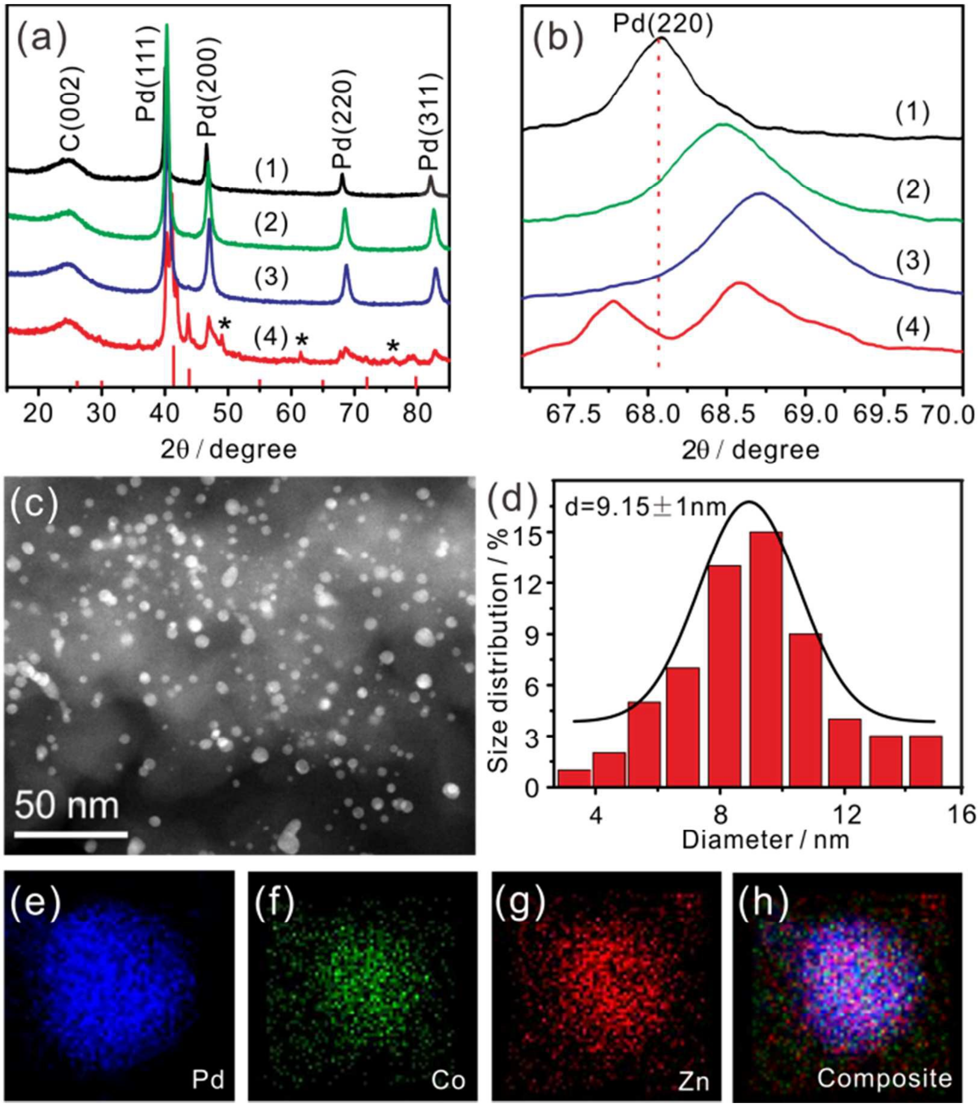

Fig. 1 (a) XRD patterns of Pd/C(1), $Pd_{12}CoZn/C$(2), Pd_8CoZn/C(3) and Pd_4CoZn/C(4). The red line and *correspond to PdZn intermetallic compound (PDF card # 03-065-9523) and Co (PDF card # 01-089-4308), respectively. (b) The enlarged region of the Pd (220) diffraction peaks in (a). The red vertical lines indicate the peak positions of the Pd (220) (PDF card # 01-089-4897). (c) Overview TEM image of Pd_8CoZn/C nanoparticles. (d) Particle size distribution of Pd_8CoZn/C. EELS elemental mapping of Pd (e), Co (f), Zn (g) and the composite of Pd, Co and Zn (h).

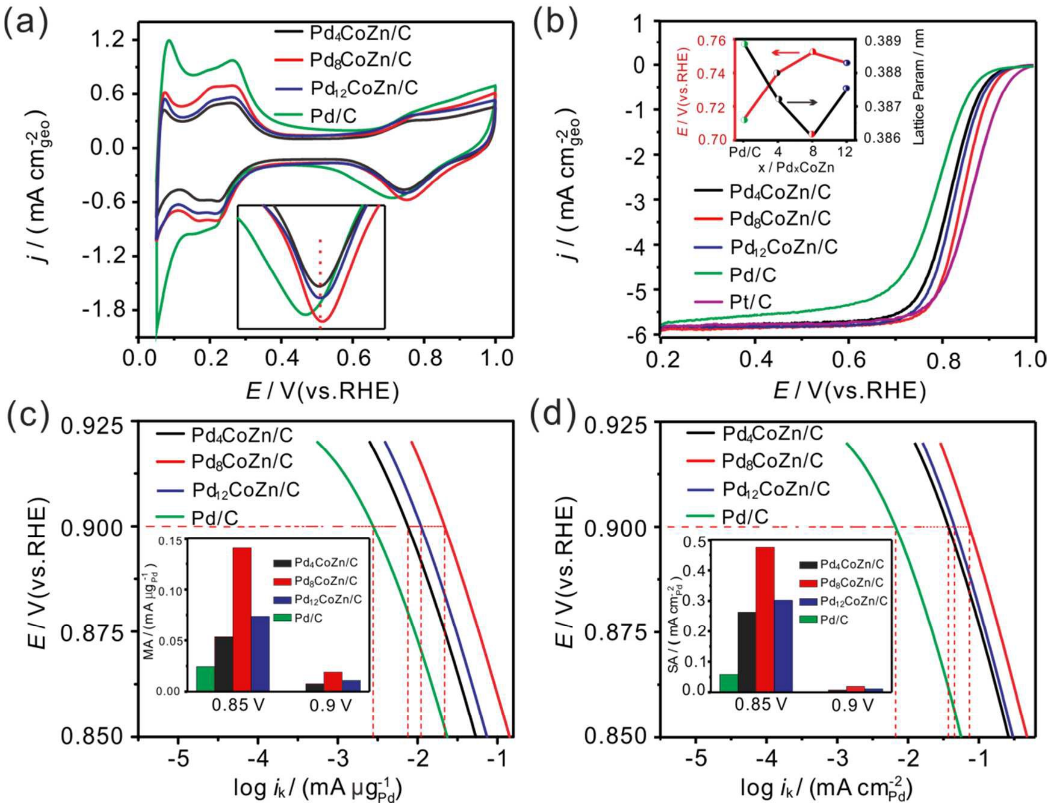

Fig. 2 (a) CVs of Pd/C and Pd$_x$CoZn/C catalysts in N$_2$-saturated 0.1 M HClO$_4$ solution at a scan rate of 50 mV s^{-1}. The insert shows the enlarged region of Pd surface oxides reduction. (b) ORR polarization curves of different catalysts in O$_2$-saturated 0.1 M HClO$_4$ solution at a sweep rate of 5 mV s^{-1} and rotation rate of 1600 rpm. The insert shows the change of peak potential of Pd surface oxides reduction and lattice parameters of Pd with the ratio of Pd and Co. (c) Mass activities and (d) Specific activities at 0.85 V and 0.9 V, respectively.

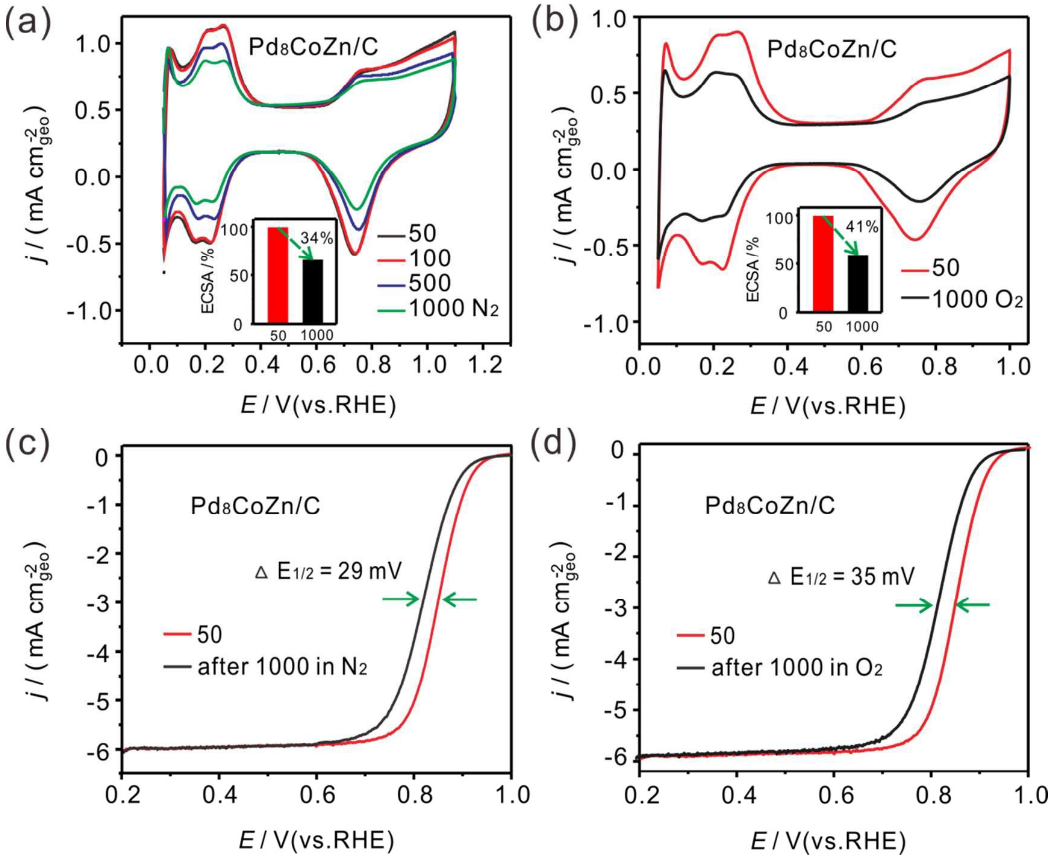

Fig. 3 (a) CVs of the Pd_8CoZn/C nanoparticles after different number of potential cycles between 0.05 V and 1.1 V in N_2-saturated 0.1 M $HClO_4$, sweep rate, 50 mV s^{-1}. The inserts show the changes of corresponding ECSA. (b) CVs changes for Pd_8CoZn/C before and after 1000 potential cycles between 0.6 V and 1.0 V in O_2-saturated 0.1 M $HClO_4$, sweep rate, 50 mV s^{-1}. The inserts show the changes of corresponding ECSA. (c) ORR polarization curves of Pd_8CoZn/C nanoparticles before and after cycling in N_2-saturated 0.1 M $HClO_4$, rotation rate, 1600 rpm; sweep rate, 5 mV s^{-1}. (d) ORR polarization curves of Pd_8CoZn/C nanoparticles before and after cycling in O_2-saturated 0.1 M $HClO_4$ between 0.6 V and 1.0 V, rotation rate, 1600 rpm; sweep rate, 5 mV s^{-1}.

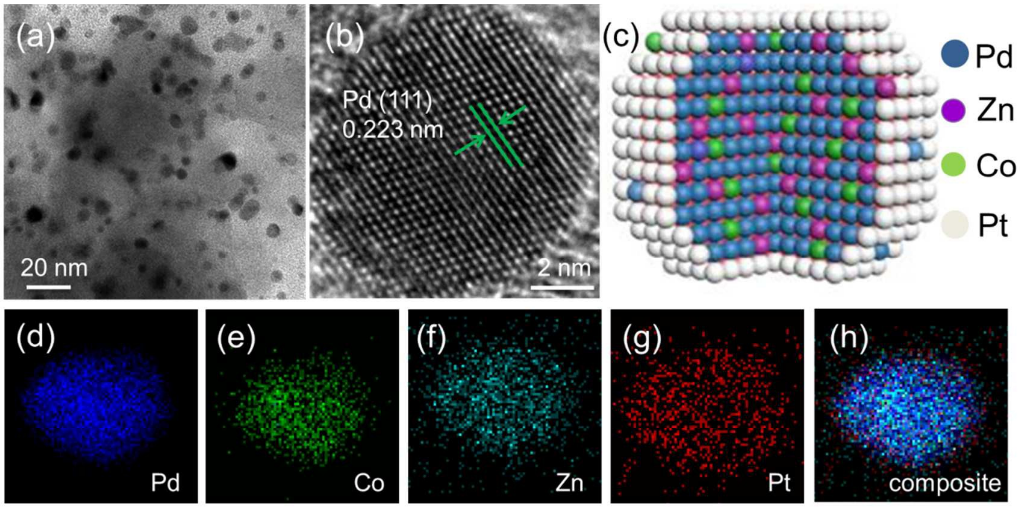

Fig. 4 (a) Overview TEM image of $Pd_8CoZn@Pt/C$ nanoparticles. (b) HRTEM image of an individual $Pd_8CoZn@Pt/C$ nanoparticle. (c) The idealized atomic structure of the $Pd_8CoZn@Pt/C$ core-shell nanoparticle. EELS elemental mapping of Pd (d), Co (e), Zn (f), Pt (g) and the composite of Pd, Co, Zn and Pt (h).

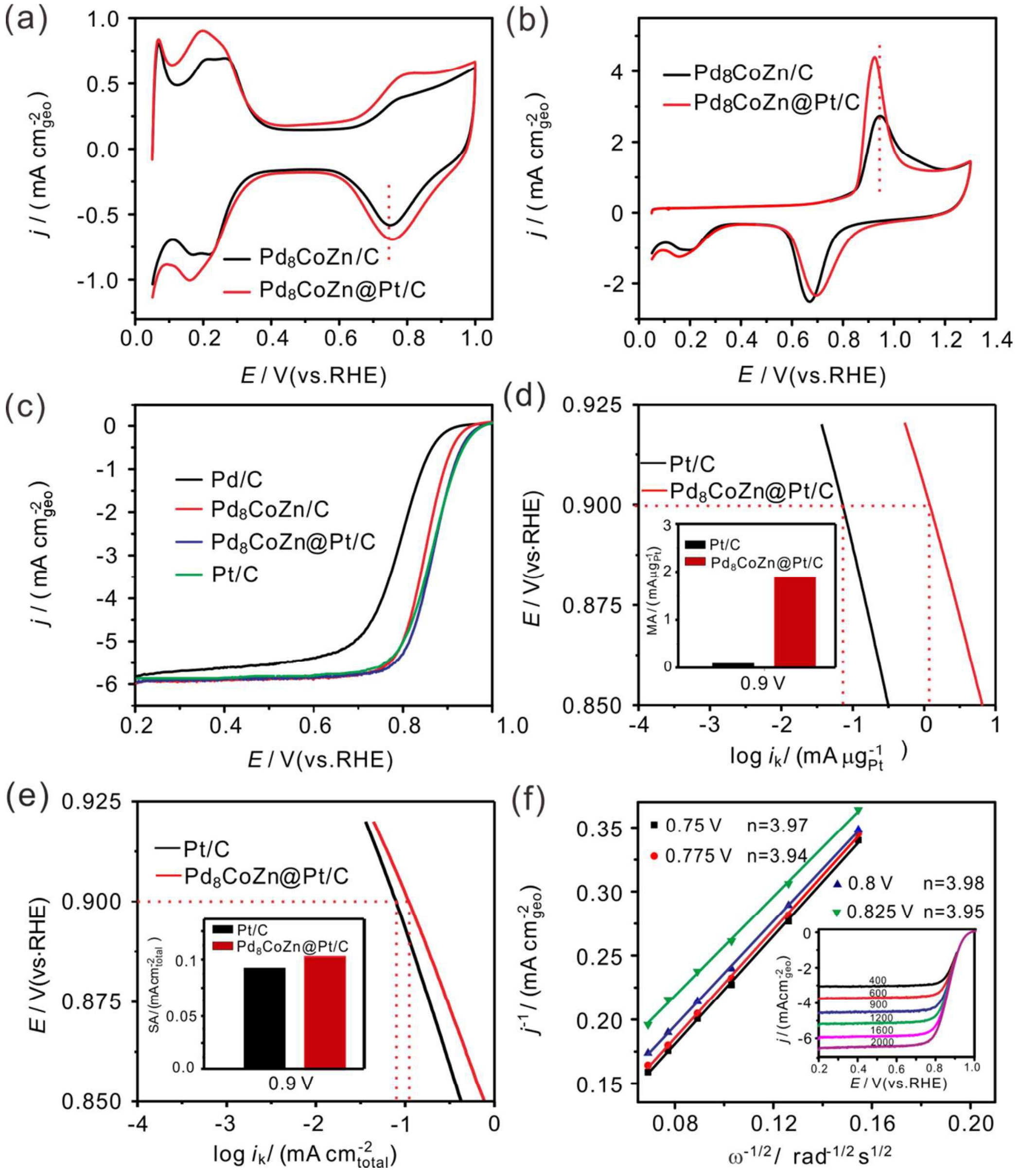

Fig. 5 (a) CVs of Pd_8CoZn/C and $Pd_8CoZn@Pt/C$ catalysts in N_2-saturated 0.1 M $HClO_4$ solution at a scan rate of 50 mV s^{-1}. (b) The CO stripping voltammetry at a scan rate of 50 mV s^{-1} in an N_2-saturated 0.1 M $HClO_4$ solution. (c) ORR polarization curves of different catalysts in O_2-saturated 0.1M $HClO_4$ solution at a sweep rate of 5 mV s^{-1} and rotation rate of 1600 rpm. MA (d) and SA (e) comparison on $Pd_8CoZn@Pt/C$ and Pt/C catalysts normalized to Pt loading of the catalyst and the ECSA, respectively. (f) The Koutecky-Levich plots on $Pd_8CoZn@Pt/C$ at different potentials. The insert shows the rotation-rate-dependent current-potential curves of

$Pd_8CoZn@Pt/C$.

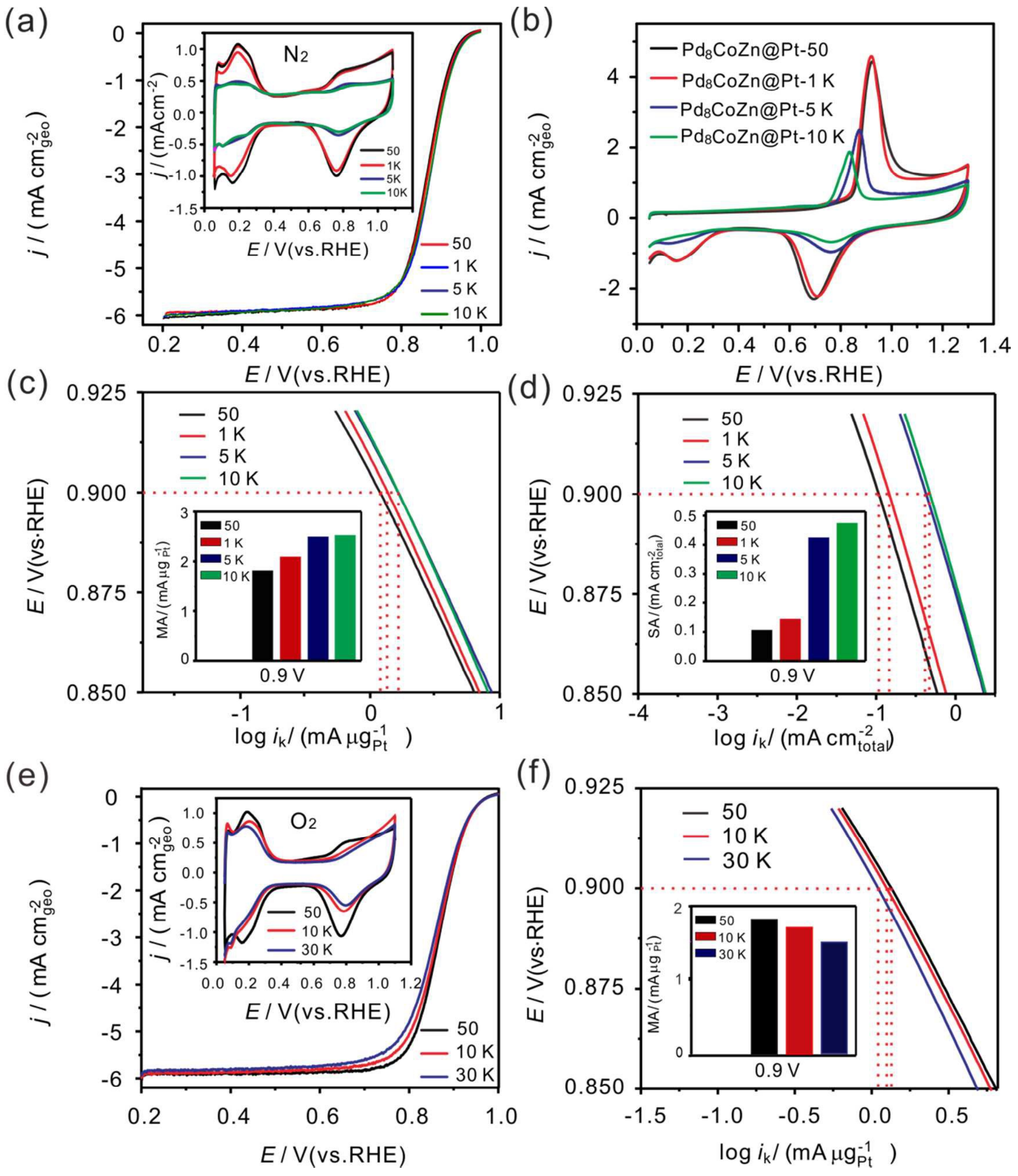

Fig. 6 (a) ORR polarization curves of $Pd_8CoZn@Pt/C$ nanoparticles before and after different potential cycles in N_2-saturated 0.1 M $HClO_4$, rotation rate, 1600 rpm; sweep rate, 5 mV s^{-1}. The insert shows the CV comparison of $Pd_8CoZn@Pt/C$ nanoparticles after different cycles between 0.05 V and 1.1 V in N_2-saturated 0.1 M $HClO_4$, sweep rate, 50 mV s^{-1}. (b) The CO stripping voltammetry of $Pd_8CoZn@Pt/C$ catalyst after different potential cycles in N_2-saturated 0.1 M $HClO_4$ solution at a scan rate of 50 mV s^{-1}. MA (c) and SA (d) comparison on $Pd_8CoZn@Pt/C$ electrode after durability

test in N_2-saturated 0.1 M $HClO_4$. The kinetic current densities (i_k) is obtained by normalizing the kinetic current to Pt loading (MA) and the ECSA (SA), respectively. (e) ORR polarization curves of $Pd_8CoZn@Pt/C$ nanoparticles before and after different potential cycles in O_2-saturated 0.1 M $HClO_4$, rotation rate, 1600 rpm; sweep rate, 5 mV s^{-1}. The insert shows the CV of the $Pd_8CoZn@Pt/C$ nanoparticles after different number of potential cycles between 0.6 V and 1.0 V in O_2-saturated 0.1 M $HClO_4$, sweep rate, 50 mV s^{-1}. (f) MA comparison on $Pd_8CoZn@Pt/C$ electrode after durability testing in O_2-saturated 0.1 M $HClO_4$. The kinetic current densities (i_k) is obtained by normalizing the kinetic current to Pt loading (MA).

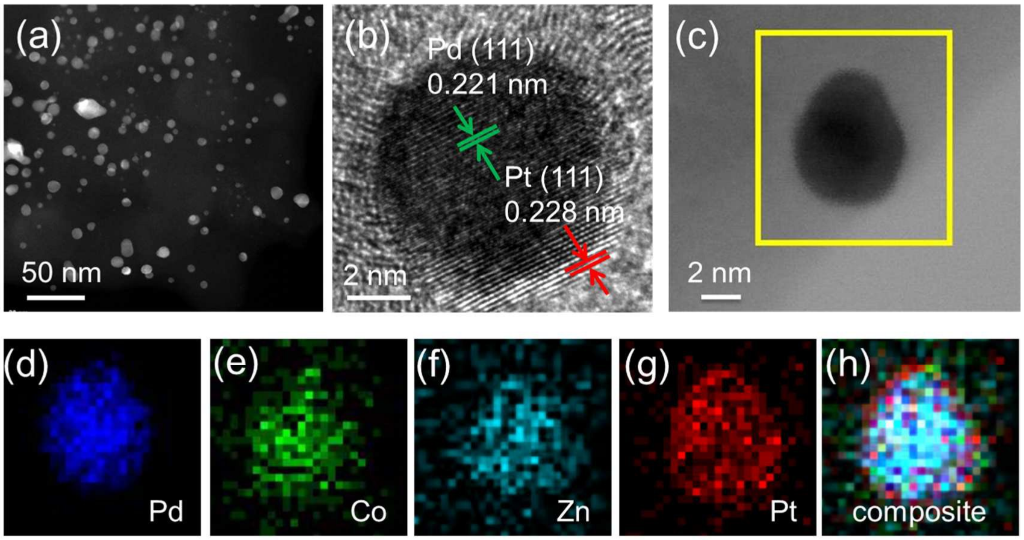

Fig. 7 (a) Overview DF-STEM image of $Pd_8CoZn@Pt/C$ nanoparticles after durability test in N_2-saturated 0.1 M $HClO_4$. (b) HRTEM image of an individual particle for $Pd_8CoZn@Pt/C$. (c) BF-STEM image of one $Pd_8CoZn@Pt/C$ nanoparticle that is spectroscopically imaged. EELS elemental mapping of Pd (d), Co (e), Zn (f), Pt (g) and the composite of Pd, Co, Zn and Pt (h).